Int. J. Electrochem. Sci., 10 **(2015)** 8783 - 8796

International Journal of
ELECTROCHEMICAL
SCIENCE
www.electrochemsci.org

Visible Light Induced Photoelectrochemical Cathodic Protection for 304 SS by In_2S_3-sensitized ZnO Nanorod Array

Jiangping Jing[1,2], *Zhuoyuan Chen*[1,*], *Yuyu Bu*[1]

[1]Key Laboratory of Marine Environmental Corrosion and Bio-fouling, Institute of Oceanology, Chinese Academy of Sciences, 7 Nanhai Road, Qingdao 266071, China
[2]University of Chinese Academy of Sciences, 19 (Jia) Yuquan Road, Beijing 100039, China
[*]E-mail: zychen@qdio.ac.cn

Received: 1 June 2015 / *Accepted:* 19 August 2015 / *Published:* 26 August 2015

The In_2S_3-sensitized ZnO nanorod array (NRA) composite was prepared using a two-step reaction method. The ZnO nanorod has a diameter of approximately 100 nm and In_2S_3 nanoparticles were grown on the ZnO NRA surface. The In_2S_3/ZnO NRA composite sintered at 400°C exhibits the best photoelectrochemical cathodic protection performance under visible light. The introducing of In_2S_3 into the In_2S_3/ZnO NRA composite results in the extension of the photoresponse of this composite to visible light, as well as the significant improvement of the separation efficiency of the photogenerated electrons and holes, and thus resulting in a dramatic increase of the photoelectrochemical cathodic protection performance of this composite.

Keywords: In_2S_3; ZnO nanorod array; photoelectrochemical cathodic protection; visible light

1. INTRODUCTION

Enormous economic losses are caused by corrosion in the globe, and the direct economic loss caused by corrosion is about 3.1% of the gross national product of the United States [1]. Except for the huge economic losses, serious environmental pollution is caused as well. Thus, it is urgent to develop the economic and environment-friendly corrosion protection technologies. It was found that the photoelectrochemical effect of semiconductors with much more negative conduction band (CB) potentials comparing to the corrosion potential of the coupled metal can be used to protect the metals from corrosion. This novel technology utilizes clean and renewable solar energy to irradiate the semiconductors for generating photoinduced electrons. The photoinduced electrons migrate into the metal surface to inhibit the anodic dissolution of the coupled metal. Importantly, the semiconductor materials will not be consumed away since they just act as photo-to-current conversion centers.

Therefore, this novel technology is a very promising environment-friendly corrosion protection method, and it has been attracting the increasing attention [2-4].

Since Honda et al. [5] reported the photoelectrochemical performance of TiO_2, the potential application of semiconductor materials, represented by TiO_2, has been widely investigated. Yuan and Tsujikawa [6] reported that TiO_2 could provide the photoelectrochemical cathodic protection for copper under UV illumination. However, the band gap of TiO_2 is wide and it only responds to UV light which accounts for only 3–4% of solar light. Furthermore, fast secondary recombination of the photogenerated electrons and holes limits the widespread application of TiO_2 [7-9]. Zinc oxide (ZnO) is an excellent substitute for TiO_2 because it is inexpensive and environmentally-friendly. Importantly, the electron mobility in ZnO is much higher than that in TiO_2. High electron mobility can effectively improve the electron transfer rate and thus can effectively inhibit the secondary recombination of the photoinduced electron-hole pairs, resulting in the significant increase of the lifetime of the photoinduced charge carriers. Meanwhile, due to its ease of crystallization and antisotropic growth, ZnO has a significant advantage of being prepared with special nanomorphologies, such as nanotubes [10,11], nanorods [12,13], nanowires [14,15] and nanosheets [16,17], which can further enhance the migration capability of the photoinduced electrons. Therefore, ZnO possesses a great application potential and it has been widely studied in many fields [18-27].

Despite the advantages of ZnO, the wide band gap (3.2 eV), which is similar with that of TiO_2, limits the widespread application of ZnO. For TiO_2, considering to utilize the solar energy more effectively, extensive work has been carried out to extend the light responsive region to visible light by preparing composites with narrow band-gap semiconductor materials. Wang et al. [28] prepared a $CdS@TiO_2$ photoelectrode and found that it could provide photoelectrochemical cathodic protection for metals under the illumination of both UV and visible light. Lin et al. [29] prepared a $ZnS/CdS@TiO_2$ thin-film photoelectrode by depositing a ZnS layer on the $CdS@TiO_2$ surface, and they found this photoelectrode can provide highly efficient photoelectrochemical cathodic protection for stainless steel. Inspiration has been stimulated for using ZnO more efficiently, namely, coupling ZnO with a narrow band gap semiconductor material such as CdS. However, the toxicity of Cd has restricted its widespread application in the field of photocatalysis. It was found that In_2S_3 is an excellent alternative semiconductor material of CdS. Among the crystalline forms of In_2S_3, β-In_2S_3 is an excellent n-type semiconductor with the band gap of 2.0-2.3 eV [30,31]. It was reported that β-In_2S_3 showed a very stable photocatalytic activity for the photoelectrochemical water splitting and the photoinduced degradation of Rhodamine B and methyl orange [32,33]. Furthermore, the CB potential of In_2S_3 is approximately -0.8 V (vs. SHE), which is more negative than the open circuit potentials (OCPs) of most of metals. Therefore, it is believed that β-In_2S_3 may provide photoelectrochemical cathodic protection for most of metals under visible light.

In the present work, ZnO nanorod array (NRA) was prepared on the fluorine-doped tin oxide (FTO) conductive glass surface by hydrothermal method and subsequently deposited a layer of In_2S_3 on the ZnO NRA surface by chemical bath deposition. The photoelectrochemical cathodic protection performance of the In_2S_3/ZnO NRA composite for 304 stainless steel (304 SS) was studied under visible light. Finally, the promotion mechanism of the photoelectrochemical cathodic protection for 304 SS by using the In_2S_3/ZnO NRA composite under visible light was proposed.

2. EXPERIMENTAL

2.1 Preparation of ZnO NRA

The preparation of ZnO NRA on the FTO conductive glass was based on the method used by Law et al. [34]. An FTO glass (10×10 mm^2) was first ultrasonically cleaned for 10 min in a liquid mixture made by acetone, isopropanol and pure water with the volume ratio of 1:1:1, and subsequently cleaned with pure water for 10 min by sonification, then rinsed with pure water and dried. The cleaned FTO conductive glass was then deposited with a ZnO nanoparticle seed layer by applying the following steps: 1.83 g zinc acetate and 1.26 g diethanolamine were dissolved in 25 mL anhydrous alcohol. A homogeneous sol was formed after stirring at 60 °C for 30 min. A dip-coating method (1 $cm \cdot min^{-1}$ pulling rate) was applied to deposit an evenly distributed sol film onto the FTO conductive glass. A even ZnO nanoparticle seed layer was then built on the FTO glass surface after heating at 500 °C for 1 h.

1.1 g zinc acetate, 0.7 g hexamethylenetetramine, 0.072 g polyethyleneimine and an appropriate amount of pure water was mixed together to form a solution with a total volume of 200 mL after stirring for 20 min in an ice bath. 35 mL of this mixed solution was then transferred to a 50-mL polytetrafluoroethylene tube. The FTO glass pre-deposited with a ZnO nanoparticle seed layer was immersed into the solution in this polytetrafluoroethylene tube. The sample was faced down, and maintained at a certain angle versus the wall of this polytetrafluoroethylene tube, and hydrothermally treated at 95 °C for 4 h. This treatment was repeated again to increase the rod length of the ZnO NRA. The second reaction time was 3 h. The prepared sample was firstly rinsed with pure water and then rinsed with anhydrous alcohol, after that, the sample was then annealed at 500 °C for 1 h. All reagents used in this work were of analytical grade from Aladin Industrial Corporation, China.

2.2 Preparation of the In_2S_3/ZnO NRA composite

In_2S_3 was grown on the ZnO NRA using chemical bath deposition by applying the following steps. The FTO glass with ZnO NRA was sequentially immersed into 0.01 $mol \cdot L^{-1}$ $In(NO_3)_3$, pure water, 0.1 $mol \cdot L^{-1}$ Na_2S and pure water for 1 min. The steps mentioned above were repeated for 10 times. The ZnO NRA was then rinsed with pure water and dried, and finally sintered at 300, 400 and 500 °C for 30 min, respectively. The In_2S_3/ZnO NRA composite was obtained. The In_2S_3/ZnO NRA composites sintered at 300, 400 and 500 °C are expressed as the In_2S_3/ZnO NRA-300, In_2S_3/ZnO NRA-400 and In_2S_3/ZnO NRA-500 composites, respectively.

2.3 Characterizations of the In_2S_3/ZnO NRA composite

The morphologies of the prepared composites were studied by a scanning electron microscope (SEM, JSM-6700F, JEOL, Tokyo, Japan). The crystalline structures of the prepared composites were analyzed using X-ray diffraction (XRD, D/MAX-2500/PC, Rigaku Co., Tokyo, Japan). The distribution of In_2S_3 on the ZnO NRA surface and the microstructure of the In_2S_3/ZnO interface were investigated using a high-resolution transmission electron microscope (HRTEM, FEI Tecnai G20, FEI

Company, USA). The elemental compositions and the bonding information of the prepared composites were studied by an energy dispersive spectrometer (EDS, FEI Tecnai G20, FEI Company, USA) and X-ray photoelectron spectroscopy (XPS, Axis Ultra, Kratos Analytical Ltd., England). The optical absorption performance of the prepared composites were studied by a UV/Vis diffuse reflectance spectrophotometer (U-41000, HITACHI, Tokyo, Japan).

2.4. Photoelectrochemical measurements

The photoelectrochemical cathodic protection performance measurements were done in a homemade experimental setup using CHI 660D electrochemical workstation (Shanghai Chenhua Instrument Co., Ltd., China). This experimental setup is composed of two coupled cells, corrosion cell and photoelectricity cell. A Nafion membrane (N-117, DuPont Co., USA) is used to connect these two cells to allow for the conduction of the solution in these two cells. A similar arrangement has been used previously [35]. The prepared In_2S_3/ZnO NRA composite thin-film photoelectrode was put into the solution in the photoelectricity cell, which is 0.25 mol·L^{-1} Na_2S + 0.35 mol·L^{-1} NaOH, and the 304 SS electrode was put into the solution in the corrosion cell, which is 3.5 wt% NaCl. The light source was a 300-W Xe arc lamp (PLS-SXE300, Beijing Changtuo Co. Ltd., Beijing, China). The photoelectricity cell is covered with tinfoil to shield light, just leaving a hole with diameter of ~3 cm, equipped with a quartz window, to pass through the light. A 420-nm cutoff filter was put in front of this quartz window to remove light with wavelengths <420 nm to generate visible light. The light was then irradiated on the back side of the In_2S_3/ZnO NRA composite thin-film photoelectrode through this quartz window. The power energy density is 150 mW·cm^{-2}.

The variations of current densities and OCPs caused by visible light illumination were tested to evaluate the cathodic protection performance of the prepared In_2S_3/ZnO NRA composites. To measure the photoinduced current density, the photoelectrode and the 304 SS electrode must be connected via a zero-resistance ammeter which allows to test the current density without polarization. To realize this test using CHI660D Electrochemical Workstation, the In_2S_3/ZnO NRA composite thin-film photoelectrode was connected to the working electrode interface of the potentiostat and the 304 SS electrode was connected to the groundwire interface of the potentiostat. The counter electrode interface of the potentiostat was connected by short circuit with the reference electrode interface of the potentiostat. In this way, the potentiostat acted as a zero-resistance ammeter and can measure the galvanic couple current with zero polarization. To measure the potentials, the In_2S_3/ZnO NRA composite thin-film photoelectrode and 304 SS electrode were also coupled with each other and connected to the working electrode interface of the potentiostat. An Ag/AgCl (saturated KCl) electrode was used as a reference electrode and was connected to the reference electrode interface of the potentiostat.

3. RESULTS AND DISCUSSION

Figure 1 shows the XRD patterns of the prepared In_2S_3/ZnO NRA composites sintered at 300 °C (Curve 1a), 400 °C (Curve 1b) and 500 °C (Curve 1c). ZnO (shown as circle), SnO_2 (shown as

triangle) and In_2S_3 (shown as square) are detected in these three composites, and In_2O_3 (shown as oval) is only found in the In_2S_3/ZnO NRA composite sintered at 500 °C.

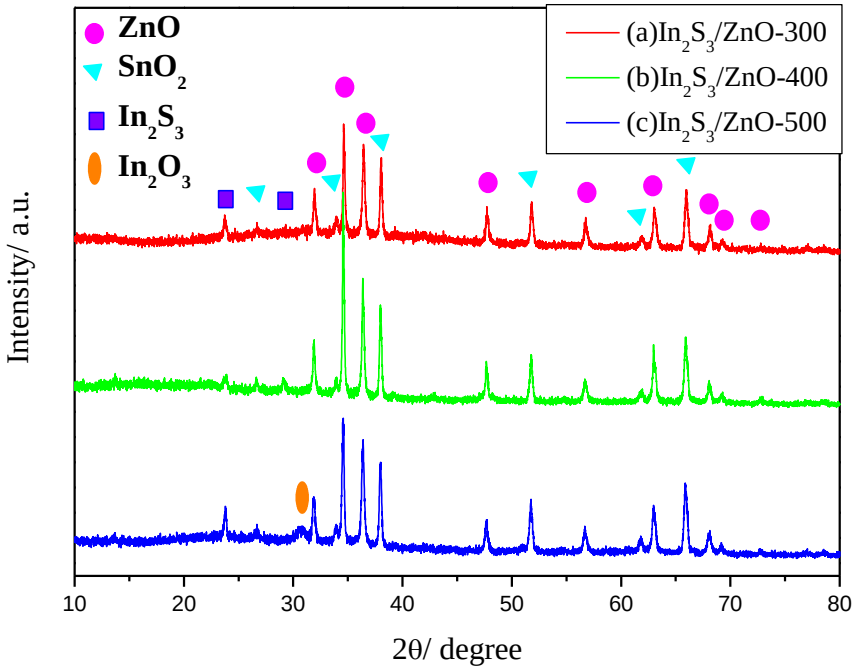

Figure 1. XRD patterns of the In_2S_3/ZnO NRA composites sintered at 300 (a), 400 (b) and (c) 500 °C.

The diffraction peaks of ZnO are clearly observed, which possess the similar crystal structure of wurtzite (JCPDS no. 36-1451). Two peaks at 2θ = 23.7° and 28.8° are observed, which can be assigned as the (220) and (222) crystal planes of In_2S_3 (JCPDS no. 32-0456). This indicates that In_2S_3 was successfully deposited on ZnO surface. SnO_2 is observed which could come from the FTO substrates. For the In_2S_3/ZnO NRA-500 composite, a peak at 2θ=30.58° is observed and this peak is assigned as the (222) crystal plane of In_2O_3 (JCPDS no. 06-0416). This may be due to the partial transformation from In_2S_3 to In_2O_3 during the sintering of the In_2S_3/ZnO NRA composite at 500 °C.

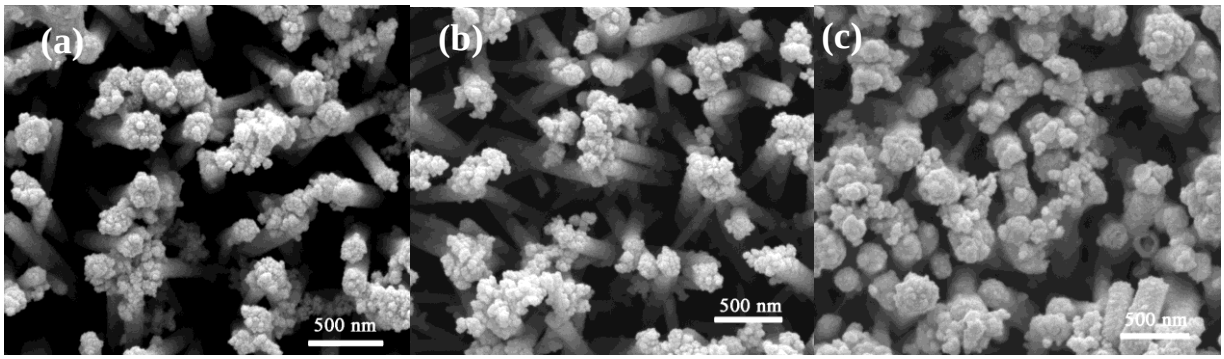

Figure 2. SEM images of the In_2S_3/ZnO NRA composites sintered at 300 (a), 400 (b) and 500 °C (c).

The morphologies of the In_2S_3/ZnO NRA composites were analyzed using SEM and the relevant results are shown in Figure 2. The nanorods with diameter of approximately 100 nm are ZnO NRA, and the sintering temperature plays little effect on the morphology of ZnO NRA. The In_2S_3 nanoparticles were successfully deposited on the ZnO nanorod surface. Additionally, there was little difference in the diameters of the In_2S_3 nanoparticles sintered at 300 °C and 400 °C. However, the agglomeration of the In_2S_3 nanoparticles can be clearly observed after sintering at 500 °C, which demonstrates that physical and chemical changes might occur in the In_2S_3 nanoparticles at this sintering temperature.

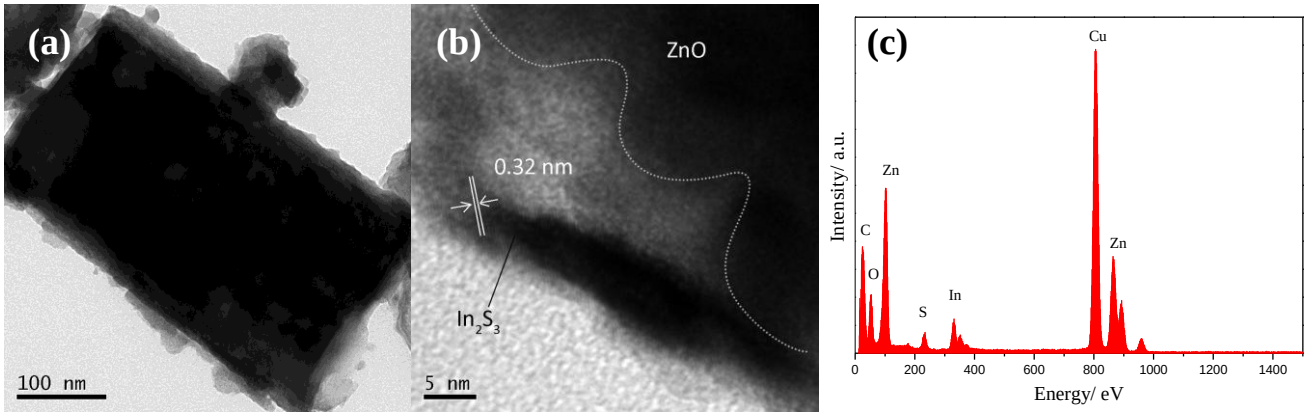

Figure 3. HRTEM morphologies of the In_2S_3/ZnO NRA composite sintered at 400 °C under low (a) and high (b) magnification, and the EDS results (c) of the In_2S_3/ZnO NRA composite sintered at 400 °C

HRTEM was employed to characterize the In_2S_3/ZnO NRA-400 composite, and the results are shown in Figure 3. As shown in the HRTEM image of the In_2S_3/ZnO NRA-400 composite obtained at low magnification (Figure 3a), a thin cladding layer and some nanoparticles of In_2S_3 are observed on the ZnO nanorod surface.

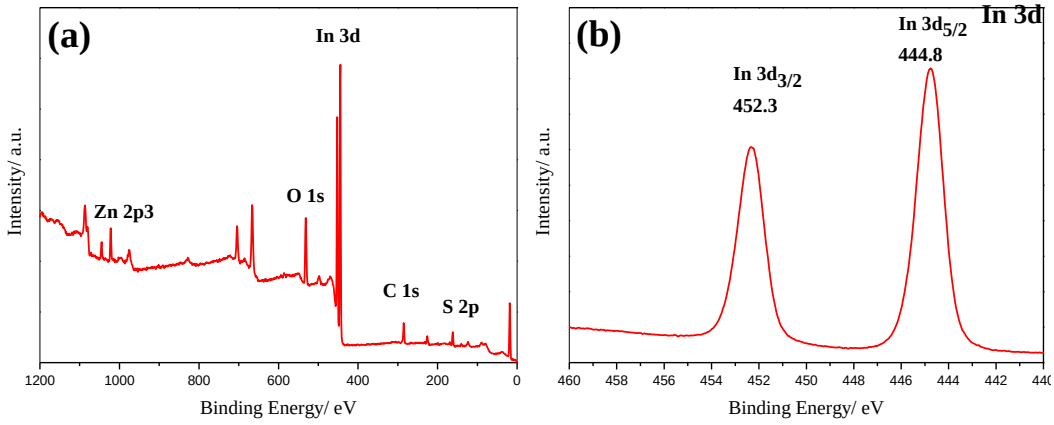

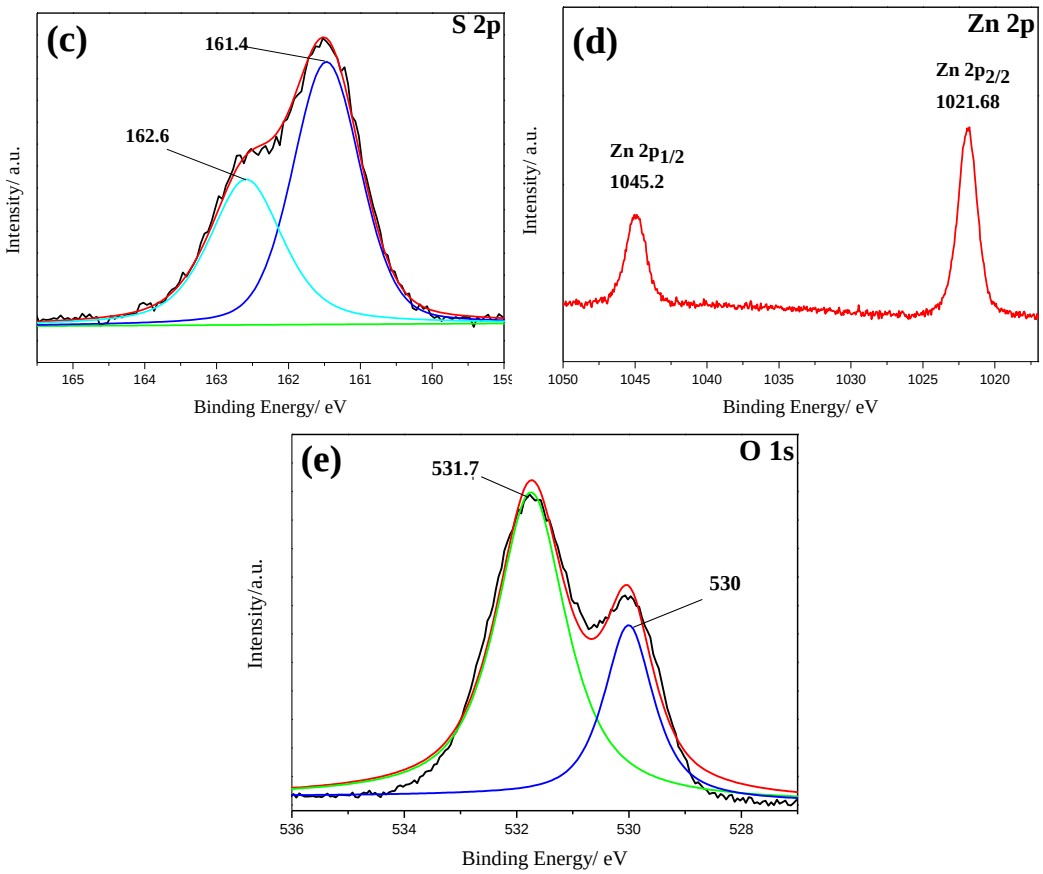

Figure 4. XPS spectra of the In_2S_3/ZnO NRA composite sintered at 400 °C. (a) the total survey spectrum, (b) the In3d XPS core level spectrum, (c) the S2p XPS core level spectrum, (d) the Zn2p XPS core level spectrum, (e) the O1s XPS core level spectrum.

HRTEM image of the In_2S_3/ZnO NRA-400 composite obtained at high magnification (Figure 3b) shows that the interface between In_2S_3 and ZnO is unclear, demonstrating that some of In_2S_3 has diffused into ZnO surface and has combined with ZnO very well. The parallel fringes with a spacing of 0.32 nm is observed, which is assigned to the (311) crystal plane of β-In_2S_3 [36]. Figure 2c shows the EDS results of the In_2S_3/ZnO NRA-400 composite, and Zn, O, In, and S elements are detected in this composite. The Cu element is obtained in Figure 2c since the EDS test was done using HRTEM with a copper mesh substrate.

XPS was used to investigate the chemical composition and states of the In_2S_3/ZnO NRA-400 composite. Figure 4a shows the total survey spectrum with the binding energy peak positions calibrated with C1s at 284.6 eV. Figure 4b shows the In3d XPS core level spectrum. The binding energy peaks at 452.3 and 444.8 eV can be assigned to the characteristics of the electron orbits of $In3d_{3/2}$ and $In3d_{5/2}$, respectively. The binding energy peaks at 161.1 and 162.2 eV are the characteristic peaks of the electron orbits of $S2p_{3/2}$ and S2p transition, respectively, as shown in Figure 4c. The XPS results are agreed with those of In_2S_3 reported in literature [37], which confirms the existence of In_2S_3 in this composite. Figure 4d shows the Zn2p XPS core level spectrum. The binding energy peaks at 1045.0 and 1021.7 eV are assigned to the electron orbits of $Zn2p_{1/2}$ and $Zn2p_{3/2}$, respectively, which can be assigned to the Z-O bonding. For the O1s XPS core level spectrum (Figure 4e), two peaks are

observed by curve fitting, in which the peak at 530 eV can be assigned to the Z-O bonding, while the peak at 531.7 eV is due to the chemically adsorbed oxygen which may come from the hydroxyl groups on the surface [38]. Considering the observation of O1s peak and Zn2p peak, ZnO can be confirmed in this composite [39]. By combining the experimental results obtained from Figures 1-4, In_2S_3 was deposited on ZnO surface. In_2O_3 was only detected on the surface of the In_2S_3/ZnO NRA composite sintered at 500 °C.

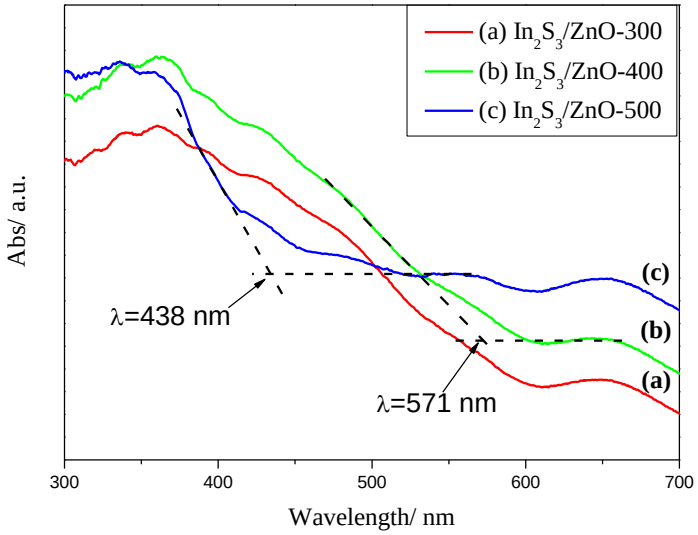

Figure 5. UV/vis diffuse reflectance spectra of the In_2S_3/ZnO NRA composites sintered at 300 (a), 400 (b) and 500 °C (c).

Figure 5 shows the UV/Vis diffuse reflectance spectra of In_2S_3/ZnO-300 (a), In_2S_3/ZnO-400 (b) and In_2S_3/ZnO-500 (c) composites. In visible light region, the In_2S_3/ZnO-400 composite exhibits the best light absorption capability. The In_2S_3/ZnO-300 composite shows weaker light absorption capability than the In_2S_3/ZnO-400 composite. This could be due to the difference of the crystallinity of In_2S_3 in the In_2S_3/ZnO-300 and In_2S_3/ZnO-400 composites. Higher crystallinity results in higher light absorption capability [40]. The crystallinity of In_2S_3 in the In_2S_3/ZnO-400 composite is much higher than that of In_2S_3 in the In_2S_3/ZnO-300 composite [41], therefore, the light absorption of the former one is higher than the latter one. However, the In_2S_3/ZnO-500 composite shows weaker light absorption capability than the In_2S_3/ZnO-400 composite. This could be due to the partial transformation from In_2S_3 to In_2O_3 during the sintering of the In_2S_3/ZnO NRA composite at 500°C. In_2O_3 has a direct band gap of 3.6 eV and an indirect band gap of 2.8 eV, which are much larger than that of In_2S_3 [42]. The larger band gap results in the blue shift of light absorption. Therefore, the In_2S_3/ZnO-500 composite shows less light absorption in visible light region. Particularly, two absorption thresholds at 571 and 438 nm are observed for the In_2S_3/ZnO-400 and In_2S_3/ZnO-500 composite, which correspond to the band gap of 2.17 and 2.83 eV, respectively. After sintered at 500 °C, the band gap of the In_2S_3/ZnO composite has increased by 0.66 eV and thus results in the decrease of the light absorption in visible light region. This is in accordance with the reports in previous reports [43-46], from which the band gap of In_2S_3 increases with the enhancing of the sintering temperature.

The photoelectrochemical cathodic protection performance of the In_2S_3/ZnO NRA composites was studied by measuring the variations of OCP and the photoinduced current density under intermittent visible light on and off. The OCP is an important parameter for judging whether a metal is cathodically protected or not. If the OCP can be shifted to negative direction under light illumination, the metal can be cathodically protected. Figure 6 shows the OCP variations of the 304 SS electrode coupled with the photoelectrodes prepared by the In_2S_3/ZnO NRA composites sintered at 300 (Curve a), 400 (Curve b) and 500 °C (Curve c) under intermittent illumination of visible light. When visible light is switched on, the 304 SS electrode coupled with the photoelectrode show a rapid potential drop, indicating that the electrons in the valence band (VB) of In_2S_3 were excited to its CB and subsequently transferred to the coupled 304 SS, leading to a potential drop of the 304 SS electrode under visible light. This is similar to the photoelectrochemical cathodic protection of TiO_2 under UV light illumination [47]. As shown in Figure 5, at the third cycle, the potential drop of 304 SS electrode coupled with the In_2S_3/ZnO-300, In_2S_3/ZnO-400 and In_2S_3/ZnO-500 thin-film photoelectrode is approximately 220, 300 and 140 mV, respectively. Obviously, the In_2S_3/ZnO-400 thin-film photoelectrode can provide the maximum potential drop under visible light.

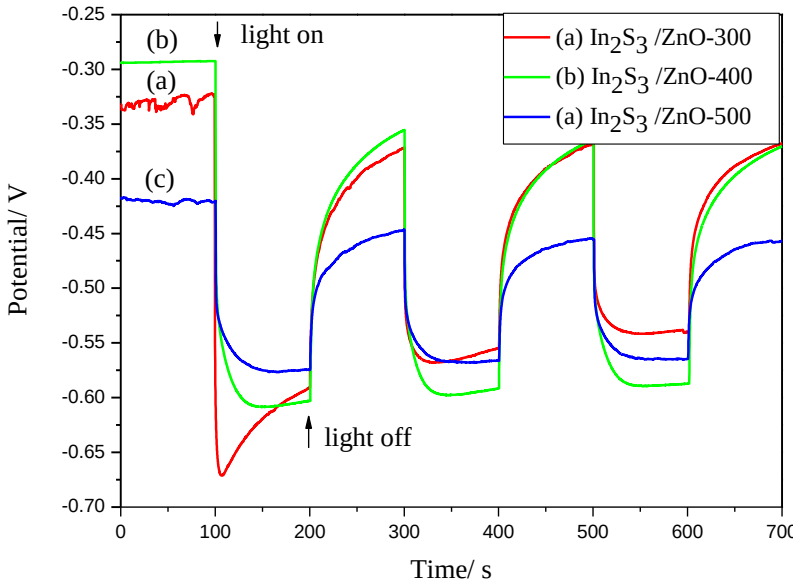

Figure 6. Variations of the open circuit potential of the galvanic coupling of the 304 SS electrode and the thin-film photoelectrodes prepared with the In_2S_3/ZnO NRA composites sintered at 300 (a), 400 (b) and 500 °C (c) under intermittent visible light illumination.

Figure 7 shows the variations of the photoinduced current densities (i-t curve) for the galvanic coupling between the prepared photoelectrode and the 304 SS electrode at a bias potential of 0 V (vs Ag/AgCl). Current densities immediately shifted to positive direction as soon as the light was switched on, as shown in Figure 7, indicating that the In_2S_3/ZnO NRA thin-film electrode acted as an anode and the 304 SS electrode acted as a cathode under light illumination. Meanwhile, the positive excitation current under light illumination demonstrated that the energies of the photoinduced electrons generated by the In_2S_3/ZnO NRA composite were high enough to overcome the energy barriers between the

In_2S_3/ZnO NRA thin-film photoelectrode and the 304 SS electrode. Thus the photoinduced electrons would transfer to the 304 SS electrode to generate a positive current and they would be consumed by the oxygen reduction at the interface between 304 SS and 3.5 wt% NaCl. These results indicated that the 304 SS was cathodically protected by the coupled photoelectrode under visible light. As shown in Figure 7, the photoelectrodes prepared by the In_2S_3/ZnO-300, In_2S_3/ZnO-400 and In_2S_3/ZnO-500 composites could provide the coupled 304 SS with about 150, 280 and 220 $\mu A \cdot cm^{-2}$ of current density under visible light illumination, respectively. More photogenerated electrons were excited to the CB of In_2S_3 under visible light for the In_2S_3/ZnO-400 composite than the In_2S_3/ZnO-300 and In_2S_3/ZnO-500 composites, letting the Fermi level of In_2S_3 move close to its CB potential. These reduced the potential of the In_2S_3/ZnO-400 thin-film photoelectrode to a much more negative level, which is in accordance with the observations for the photoinduced OCPs shown in Figure 6. Meanwhile, higher photoinduced current density can polarize the coupled 304 SS electrode to a much more negative potential and thus provide much better cathodic protection for it. The results obtained in Figures 6 and 7 indicate that the In_2S_3/ZnO-400 composite can provide the largest potential drop (~300 mV) and the biggest photoinduced current density (~280 $\mu A \cdot cm^{-2}$), demonstrating that the In_2S_3/ZnO-400 composite possesses the best photoelectrochemical cathodic protection performance under visible light.

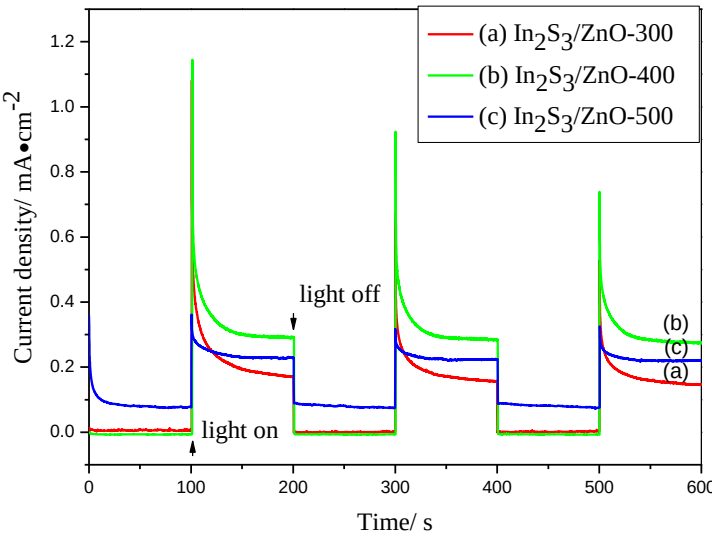

Figure 7. Variations of the current densities with time for the thin-film photoelectrodes prepared with the In_2S_3/ZnO NRA composites sintered at 300 (a), 400 (b) and 500 °C (c) coupled with the 304 SS electrode under intermittent illumination by visible light.

Shazly et al. [41] reported that the crystallinity of In_2S_3 increased with the increase of the sintering temperature. In this work, the crystallinity of In_2S_3 in the In_2S_3/ZnO-400 composite should be much higher than that of In_2S_3 in the In_2S_3/ZnO-300 composite. High crystallinity of the semiconductor would result in a higher photovoltaic effect, and thus can generate much better photoelectrochemical cathodic protection performance [48]. This is in good agreement with the UV/Vis result, which the In_2S_3/ZnO-400 composite shows higher visible light absorption capability

than the In_2S_3/ZnO-300 composite. However, the In_2S_3/ZnO-500 composite can provide much weaker photoelectrochemical cathodic protection performance than the In_2S_3/ZnO-400 composite although the crystallinity of In_2S_3 in the In_2S_3/ZnO-500 composite will be much higher than that of In_2S_3 in the In_2S_3/ZnO-400 composite. This could be caused by the formation of In_2O_3 in the In_2S_3/ZnO-500 composite. As reported by Datta et al. [49], In_2S_3 partially transformed to In_2O_3 at the sintering temperature of > 400 °C, and In_2O_3 was totally formed after sintering at 600 °C. In this work, In_2O_3 was only detected in the In_2S_3/ZnO-500 composite, and it was not observed in the In_2S_3/ZnO-300 and In_2S_3/ZnO-400 composites. The light absorption capability of In_2O_3 is much weaker than that of In_2S_3 in visible light region, resulting in the weaker light absorption capability of the In_2S_3/ZnO-500 composite than that of the In_2S_3/ZnO-400 composite in visible region. The increased light absorption implies that more optical energy can be utilized to protect the coupled 304 SS by the In_2S_3/ZnO-400 composite, resulting in a much better photoelectrochemical cathodic protection performance of the In_2S_3/ZnO-400 composite.

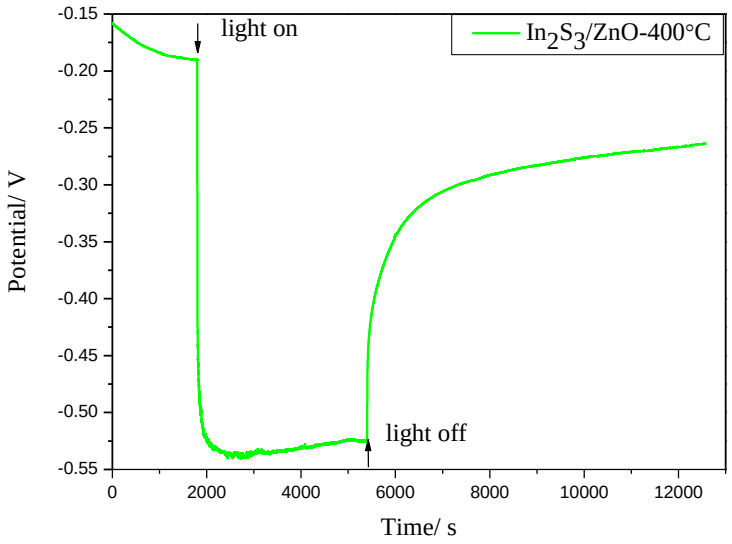

Figure 8. Changes in the open circuit potential of the 304 SS electrode coupled with the thin-film photoelectrode prepared with the In_2S_3/ZnO NRA composite sintered at 400 °C under 1 h visible light illumination and subsequently 2 h in the dark.

The stability of the photoelectrochemical carhodic protection performance of the In_2S_3/ZnO-400 composite was investigated by monitoring the potential changes of the 304 SS electrode coupled with the In_2S_3/ZnO-400 thin-film photoelectrode under a 1-h illumination by visible light. Figure 8 shows the OCP changes of the 304 SS electrode coupled with the In_2S_3/ZnO-400 thin-film photoelectrode under 1 h visible light illumination and subsequently 2 h in the dark. As shown in Figure 8, the OCP of the 304 SS electrode immediately decreases as soon as the visible light was switched on, similar with that observed in Figure 6. The potential of 304 SS keeps being stable during the 1-h illumination by visible light, demonstrating that the In_2S_3/ZnO-400 composite can provide very stable photoelectrochemical cathodic protection for 304 SS under visible light illumination.

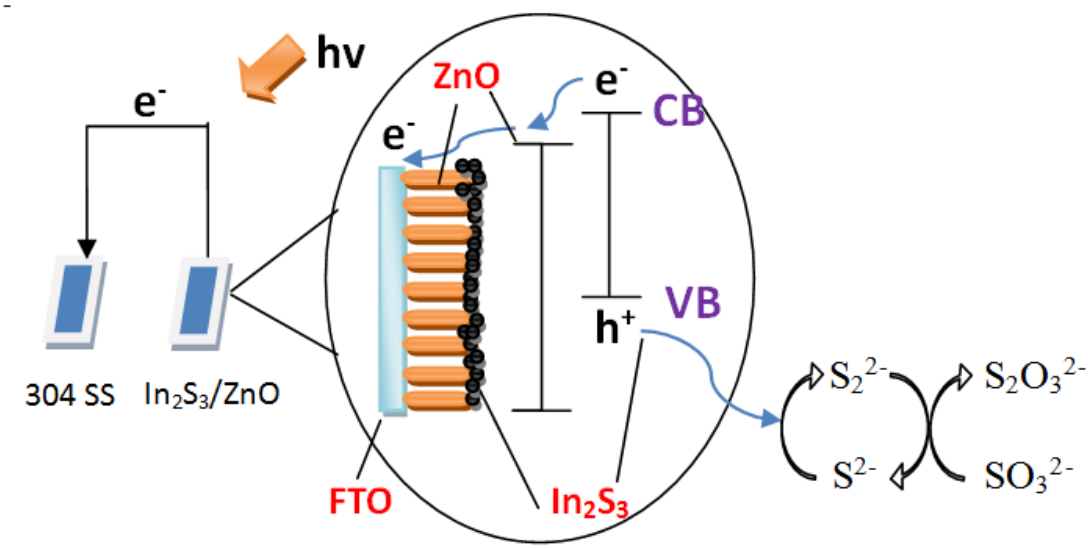

Figure 9. Schematic illustrations of the mechanism of the photoelectrochemical cathodic protection for 304 SS using the In_2S_3/ZnO NRA composite thin-film photoelectrode.

Figure 9 schematically illustrates that the proposed mechanism of the photoelectrochemical cathodic protection for 304 SS using the In_2S_3/ZnO-400 thin-film photoelectrode. As we know, the CB potential of ZnO is more positive than that of In_2S_3 [50]. The electrons in the valance band of In_2S_3 are excited to its CB under visible light illumination and they can transfer to the CB of ZnO since the CB potential of ZnO is more positive than that of In_2S_3. Because the CB potential of In_2S_3 is more negative than the Fermi level of 304 SS, the photoinduced electrons generated by In_2S_3 will finally transfer to the coupled 304 SS, resulting in the cathodic protection for the coupled 304 SS. Meanwhile, the valence band potential of ZnO is more positive than that of In_2S_3. Therefore, the photoinduced holes generated by In_2S_3 cannot transfer to ZnO, and they will finally transfer to the In_2S_3 surface and will then rapidly oxidize S^{2-} ions to join the formation cycle of polysulphides.

4. CONCLUSIONS

In this work, the In_2S_3/ZnO NRA composite was prepared using a two-step method. The introducing of In_2S_3 into the In_2S_3/ZnO NRA composite extends the light absorption range into the visible region and makes the In_2S_3/ZnO NRA composite has the visible light responsive activity. The photoelectrochemical cathodic protection performance of the In_2S_3/ZnO NRA composite is related to the sintering temperature and the In_2S_3/ZnO NRA composite sintered at 400 $^{\circ}$C possesses the best photoelectrochemical cathodic protection capability. Under visible light illumination, the OCP of 304 SS can decrease approximately 300 mV due to the photovoltaic effect of the In_2S_3/ZnO-400 composite, and the photoinduced current density generated by this composite is approximately 280 $\mu A \cdot cm^{-2}$.

ACKNOWLEDGEMENTS
The authors appreciate the financial support from the National Natural Science Foundation of China (Grant No. 41376126) and the Hundreds-Talent Program of the Chinese Academy of Sciences (Y02616101L).

References

1. B.A. Shaw, R.G. Kelly, *The Electrochemical Society Interface spring* (2006) 24-26.
2. G. X. Shen, Y. C. Chen, C. J. Lin, *Thin Solid Films* 489 (2005) 130-136.
3. C. X. Lei, Z. D. Feng, H. Zhou, *Electrochim. Acta* 68 (2012) 134-140.
4. X. Q. Guo, W. Liu, L. X. Cao, G. Su, H. M. Xu, B. H. Liu, *Appl. Surf. Sci*. 283 (2013) 498-504.
5. A. Fujishima, K. Honda, *Nature* 238 (1972) 37-38.
6. J. Yuan, S. Tsujikawa, *J. Electrochem. Soc*. 142 (1995) 3444-3450.
7. M. Ni, M. K. H. Leung, D. Y. C. Leung, K. Sumathy, Renewable Sustainable Energ. Rev. 11 (2007) 401-425.
8. Y. Li, J. Z. Zhang, *Laser Photonics Rev*. 4 (2010) 517-528.
9. M. G. Walter, E. L. Warren, J. R. McKone, S. W. Boettcher, Q. X. Mi, E. A. Santori, N. S. Lewis, *Chem. Rev.* 110 (2010) 6446-6473.
10. Y. Hou, X. Y. Li, X. J. Zou, X. Quan, G. H. Chen, *Environ. Sci. Technol*. 43 (2009) 858-863.
11. G. Dai, J. Yu and G. Liu, *J. Phys. Chem*. C, 115 (2011) 7339-7346.
12. B. Liu, E. S. Aydil, *J. Am. Chem. Soc*. 131 (2009) 3985-3990.
13. V. A. Antohe, M. Mickan, F. Henry, R. Delamare, L. Gence, *Appl. Surf. Sci*. 313 (2014) 607-614.
14. B. Yin, Y. Qiu, H. Q. Zhang, J. X. Lei, J. Y. Ji, L. P. Li, L. Z. Hu, *Appl. Surf. Sci*. 311 (2014) 621-625.
15. G. Wang, X. Yang, F. Qian, J. Z. Zhang, Y. Li, *Nano Lett*.10 (2010) 1088-1092.
16. S. Bayan, P. Chakraborty, *Appl. Surf. Sci*. 303 (2014) 233-240.
17. F. Xu, M. Dai, Y. Lu, L. Sun, *J. Phys. Chem. C*, 114 (2010) 2776-2782.
18. W. T. Jiang, C. T. Wu, Y. H. Sung, J. J. Wu, *ACS Appl. Mater. Interfaces*, 5 (2013) 911-917.
19. K. Maeda, T. Takata, M. Hara, N. Saito, Y. Inoue, H. Kobayashi, K. Domen, *J. Am. Chem. Soc*. 127 (2005) 8286-8287.
20. A. Wolcott, W. A. Smith, T. R. Kuykendall, Y. Zhao, J. Z. Zhang, *Adv. Fun. Mater*. 19 (2009) 1849-1856.
21. X. Yang, A. Wolcott, G. Wang, A. Sobo, R. C. Fitzmorris, F. Qian, J. Z. Zhang, Y. Li, *Nano Lett*. 9 (2009) 2331-2336.
22. W. J. Han, L. Ren, X. Qi, Y. D. Liu, X. L. Wei, Z. Y. Huang, J. X. Zhong, *Appl. Surf. Sci*. 299 (2014) 12-18.
23. A. E. Rakhshani, *Appl. Surf. Sci*. 258 (2012) 9018-9025.
24. H. Qin, W. Li, Y. Xia, T. He, *ACS Appl. Mater. Interfaces* 3 (2011) 3152-3156.
25. Z. H. Li, E. S. Cho, S. J. Kwon, *Appl. Surf. Sci*. 314 (2014) 97-103.
26. K. M. Parida, S. S. Dash, D. P. Das, *J. Coll. Inter. Sci*. 98 (2006) 787-793.
27. C. H. Seager, W. L. Warren, D. R. Tallant, J. A. Voigt, *Appl. Phys. Lett.* 68 (1996) 403-405.
28. C. L. Wang, L. Sun, H. Yun, J. Li, Y. K. Lai, C.J. Lin, *Nanotechnology* 20 (2009) 295601.
29. Z. Q. Lin, Y. K. Lai, R. G. Hu, J. Li, R. G. Du, C. J. Lin, *Electrochim. Acta* 55 (2010) 8717-8723.
30. T. Asikainen, M. Ritala, M. Leskela, *Appl. Surf. Sci*. 82 (1994) 122-125.
31. W. T. Kim, C. D. J. Kim, *J. Appl. Phys*. 60 (1986) 2631-2632.
32. W. Z. Wang, W. Zhu, L. Zhang, *Research on Chemical Intermediates* 35 (2009) 761-767.
33. Y. H. He, D. Z. Li, G. C. Xiao, W. Chen, Y. B. Chen, M. Sun, H. J. Huang, X. Z. Fu, *J. Phys. Chem.* 113 (2009) 5354.
34. M. Law, L. E. Greene, J. C. Johnson, R. Saykally, P. Yang, *Nat. Mater.* 4 (2005) 455-459.

35. Y. Y. Bu, Z. Y. Chen, J. Q. Yu, W. B. Li, *Electrochim. Acta*. 88 (2013) 294-300.
36. M. M. El-Nahass, B. A. Khalifa, H. S. Soliman, M. A. M. Seyam, *Thin Solid Films* 515 (2006) 1796-1801.
37. X. L. Fu, X. X. Wang, Z. X. Chen, Z. Z. Zhang, Z. H. Li, D. Y. C. Leung, L. Wu, X. Z. Fu, *Appl. Catal. B* 95 (2010) 393-399.
38. L. Q. Jing, Z. L. Xu, X. J. Sun, J. Shang, W. M. Cai, *Appl. Surf. Sci*. 180 (2001) 308-314.
39. T. G. Xu, L. W. Zhang, H. Y. Cheng, Y. F. Zhu, *App. Catal. B: Environ*. 101 (2011) 382-387.
40. Q. H. Zhang, L. Gao, J. K. Guo, *Applied Catalysis B: Environmental* 26 (2000) 207-215.
41. A. A. El-Shazly, D. A. El Hady, H. S. Metwaly, M. A. M. Seyam, *J. Phys. Condens. Matter* 10 (1998) 5943-5954.
42. P. D. C. King, T. D. Veal, F. Fuchs, Ch. Y. Wang, D. J. Payne, A. Bourlange, H. Zhang, G. R. Bell, V. Cimalla, O. Ambacher, R. G. Egdell, F. Bechstedt, C. F. McConville, *Phys. Rev*. B 79 (2009) 205-211.
43. N. Barreau, S. Marsillac, D. Albertini, J.C. Bern`ede, *Thin Solid Films* 331 (1992) 403-404.
44. N. Barreaau, S. Marsillac, J.C. Bernede, *Vacuum* 56 (2000) 101-106.
45. K. Bouabid, A. Ihlal, Y. Amira, A. Sdaq, A. Outzourhit, G. Nouet, *Eur. Phys. J. Appl. Phys*. 40 (2007) 149-154.
46. N. Barreaau, S. Marsillac, J.C. Bern`ede, A. Barreau, *Appl. Surf. Sci*. 161 (2000) 20-26.
47. Y. Ohko, S. Saitoh, T. Tatsuma and A. Fujishima, *J. Electrochem. Soc.* 148 (2001) B24-B28.
48. K. Tanaka, M. F. V. Capule, T. Hisanaga, *Chemical Physics Letters* 187 (1991) 73-76.
49. A. Datta, S. K. Panda, D. Ganguli, P. Mishra, S. Chaudhuri, *Crystal Growth and Design* 7 (2007) 163-169.
50. S. Khanchandani, S. Kundu, A. Patra, A. K. Ganguli, *Phys. Chem.* C 117 (2013) 5558-5567.